Texas A&M University
Mechanical Engineering Department
Turbomachinery Laboratory
Tribology Group

Measurement of Structural Stiffness and Damping in a Metal Mesh Foil Bearing and Development of a Test Rig for Gas Foil Bearings

Research Progress Report to the TAMU Turbomachinery Research Consortium

TRC-B&C-5-08

By

Luis San Andrés

Mast-Childs Professor

Principal Investigator

Tae-Ho Kim

Research Associate

Thomas Abraham Chirathadam   **Alex Martinez**
Research Assistant   UG Student Worker

June 9, 2008

TEES # 32513/1519 V2

EXECUTIVE SUMMARY

Measurement of Structural Stiffness and Damping in a Metal Mesh Foil Bearing and Development of a Test Rig for Gas Foil Bearings

Metal Mesh Foil Bearings (MMFBs) are a cost effective gas bearing technology for use in oil-free microturbomachinery. These bearings will ensure low friction, long operating life, and with significant material damping for mechanical energy dissipation. In a MMFB, a donut shaped metal mesh (MM) provides a soft support to a smooth top foil wrapped around a rotating journal. The report details the construction of a MMFB and static and dynamic load tests conducted on the bearing for estimation of its structural stiffness and material damping coefficient. The MMFB, 28.15 mm in diameter and 28.05mm in length, is made of 0.3 mm Copper wire with a compactness of 20 %. The static load versus bearing deflection measurements, conducted on a stationary shaft, 28.08 mm in diameter, evidence a typical cubic nonlinearity with large hysteresis, thus leading to a hardening structural stiffness, quite distinct during both loading and unloading processes. Shaker loads of controlled amplitude and over a frequency range act on the test bearing. The dynamic bearing displacements show a single frequency, equal to that of the applied load. Analysis of the applied force and displacements in the frequency domain renders the bearing mechanical impedance, whose real and imaginary parts determine the bearing stiffness and damping coefficients, respectively. The MMFB structural stiffness decreases significantly with the amplitude of motion and, a little less, as the excitation frequency increases. The MMFB equivalent viscous damping is both frequency and amplitude dependent, decreasing rapidly with both parameters. On the other hand, a structural loss factor (material damping) represents best the mechanical energy dissipation characteristics of the test MMFB. The measurements show a loss factor as high as 0.50, a significant magnitude

for the simple mechanical system, and with little dependency on the excitation frequency. Empirically based formulas, properly modified as per the test MMFB material density, predict stiffness and damping coefficients agreeing well with the experimentally derived coefficients.

The report also describes progress on the construction of a test rig for demonstration of high speed prototype miniature gas foil bearings. A ball-bearing supported turbocharger (TC), donated by a TRC member, drives the system to a top speed of 110 krpm. The test bearing section replaces the compressor impeller and volute of the original TC. A 28 mm diameter journal, 55 mm in length, and mounted in the free end of the transmission shaft, will carry the test gas bearing. A centering elastic support, affixed to a two axes positioning table with electronic control, also holds the test gas bearing cartridge. The bearing support structure has eddy current sensors to record journal dynamic displacements, and ad-hoc mechanisms to impose a static load on the bearing and to measure the rotor lift off speed and drag torque. Upon construction completion, end of 2008, experiments will be conducted to measure the rotordynamic performance and endurance of MMFBs for high speed operation.

Note: The P.I. revised and edited <u>thirteen times</u> the report, as per language and technical content, prior to its release to TRC members.

TABLE OF CONTENTS

NOMENCLATURE

C	Metal mesh bearing equivalent viscous damping coefficient [Ns/m]
C_A	Axial compression [mm]
D_{Bi}	Bearing cartridge inner diameter [m]
D_{Bo}	Bearing cartridge outer diameter [m]
D_J	Journal diameter [m]
D_{MMi}	Metal mesh donut inner diameter [m]
D_{MMo}	Metal mesh donut outer diameter [m]
D_W	Metal wire diameter [m]
E	Young's Modulus [N/m^2]
E_{equiv}	Equivalent Modulus of Elasticity [N/m]
F	Static force [N]
$f(t)$	Dynamic force [N]
$\bar{F}$	Dynamic force in frequency domain [N]
H_{equiv}	Equivalent hysteresis damping parameter [Ns/m]
K	Metal mesh bearing structural stiffness [N/m]
L	Bearing axial length [m]
L_J	Journal axial length [m]
M	Bearing mass[kg]
M_m	Metal mesh donut mass [kg]
R_i	Metal mesh donut inner radius [m]
R_o	Metal mesh donut outer radius [m]
R_p	Radial interference [mm]
T_{tf}	Top foil thickness [m]
X	Bearing static displacement [m]
$x(t)$	Bearing dynamic displacement [m]
$\bar{X}$	Bearing dynamic displacement in frequency domain [m]
Z	Impedance [N/m]
ρ_{MM}	Wire density = metal mesh mass/ (metal mesh volume× density of metal)
υ	Poisson's Ratio
γ	Metal mesh bearing structural loss factor
ω	Frequency of excitation [rad/s]

I. INTRODUCTION

Oil-free microturbomachinery (< 250 kW) relies on gas bearings to ensure low friction and long operating life with little maintenance [1]. Metal Mesh Foil Bearings comprise of a top foil supported on a donut shaped metal mesh (MM) providing structural stiffness and material hysteresis or dry-friction for mechanical energy dissipation [2]. Metal Mesh Foil Bearings (MMFBs) aim to satisfy the requirements for light, high power density (power per unit mass) gas turbines such as automobile turbochargers, due to their simple construction and oil-free reliable high speed operation. MMFBs are a type of self-acting hydrodynamic gas bearings that use air as the lubricating fluid. A hydrodynamic film pressure builds up within the small gap between the rotating shaft and the smooth top foil, thus providing a load capacity.

The present research on MMFBs modifies a patented gas bearing with an elastic porous material under a smooth top foil [3]. Figure 1 from Ref. [3] shows that the bearing consists of a bearing cartridge (a), an external circular (cartridge shim) foil (b), a resilient porous material support (c), and a top circular smooth foil (d). The trailing edges of the top circular foil, porous material and external circular (cartridge shim) foil are pinned at (g) and the top foil leading edges are free. The external circular (cartridge shim) foil facilitates seamless installation of the porous material inside the bearing cartridge. As the rotor (e) speed increases, a hydrodynamic film pressure (f) builds up and separates the rotor from the top foil.
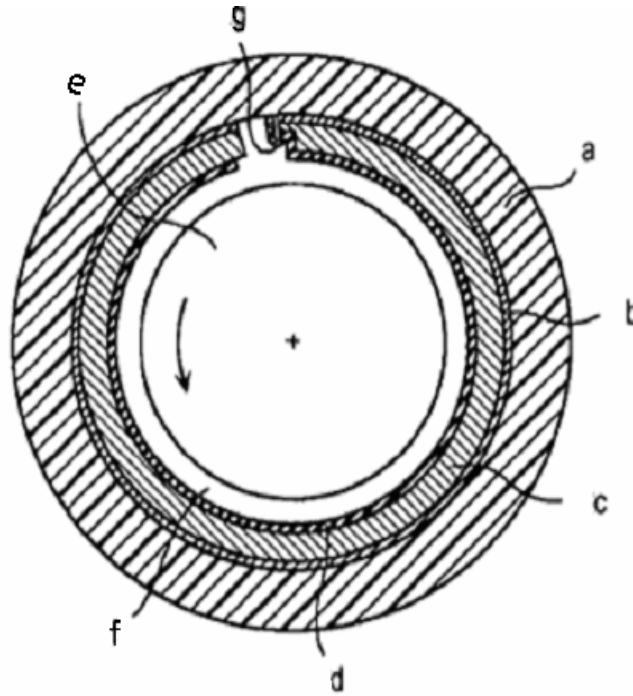
Figure 1. Air foil bearing with a porous material support [3], (a) bearing cartridge, (b) external circular (cartridge shim) foil, (c) porous material support, (d) top circular foil, (e) rotating shaft, (f) hydrodynamic air film and (g) pinned edge. Patent No. WO 2006/043736 A1

The current development follows the concept design shown in Fig. 1, but installs a commercially available metal mesh donut between the top foil and the bearing cartridge to provide structural stiffness and damping. Note that prior experiments conducted at the Turbomachinery laboratory (TL) have demonstrated that metal mesh materials have sufficient equivalent viscous damping to replace oil-lubricated squeeze film dampers, for example [4].

The report introduces a Metal Mesh Foil Bearing (MMFB), details its construction method, presents experimentally identified structural stiffness and viscous damping coefficients validating model predictions, and describes a turbocharger (TC) driven MMFB rotordynamic test rig under construction.

II. LITERATURE REVIEW

Since 1980, feasibility studies to use metal mesh material as a vibration isolator [5] in gas turbine engines have been published. A donut shaped metal mesh damper, installed in series with the outer race of an engine bearing, can provide a soft support to the turbine shaft without the need of extra space for squirrel cages, for example. Recent studies [4] also demonstrate that donut shaped metal mesh dampers provide equivalent viscous damping as large as that of oil-lubricated squeeze film dampers. The major advantage of metal mesh damper is its usability in high and low temperatures, as opposed to lubricants. The following summarizes literature on metal mesh vibration isolators and dampers.

Okayasu et al. [6] report one of the earliest usages of metal mesh, as a flexible bearing support in a liquid hydrogen turbopump, controlling subsynchronous instability, arising due to dry friction between rotating parts, and reducing high level of vibrations while traversing critical speeds. The turbopump is designed to operate above its third critical speed of 46,139 rpm. In the absence of metal mesh dampers, high vibration levels (80-150 μm pk-pk) are measured while crossing the first and second critical speeds. Introduction of metal mesh dampers into the rotor-bearing system attenuated rotor vibrations, synchronous and subsynchronous.

Zarzour [4] introduces a stainless steel mesh damper replacing a squeeze film damper (SFD) as an effective damping element. Experiments in a test rig replicating a power turbine demonstrate that the viscous damping coefficient of the metal mesh damper is comparable to that of SFDs. The viscous damping coefficient of the metal mesh damper does not change significantly for tests covering a temperature range of 54°C-99°C, proving its reliability as a damping element in this temperature range. However, the stiffness decreases (softening effect) with an increase in operating temperature. Also, the imbalance response amplitude at the rotor-bearing system critical speed does not change when the metal mesh is drenched in oil. Note that the metal mesh damper shows, during static load tests, a peculiar behavior with linear loading

and non-linear unloading features. That is, during loading, the metal mesh donut deflection is linear; and during unloading, the metal mesh donut deflection is nonlinear.

Another feature of a metal mesh damper is the ability to retain its damping when assembled in conjunction with other stiffening elements. Al-Khateeb and Vance [7] report that a donut shaped metal mesh damper in parallel with a squirrel cage allows varying the support stiffness without any effect on its equivalent viscous damping. Ertas et al. [8] investigate the usefulness of metal mesh as bearing dampers at cryogenic temperatures, reporting an increase in metal mesh damper stiffness with a decrease in temperature for both steel and copper meshes. The equivalent viscous damping coefficient of a steel mesh damper does not change with temperature. Equivalent viscous damping increases significantly for a copper mesh damper with a decrease in temperature, achieving its highest value at the lowest test temperature of -190°C. The selection of the mesh material depends mainly on the damping it provides. Burshid [9] reports using a copper mesh for auxiliary sealing in a hybrid damper seal design. Tests show that a copper wire mesh has more damping than a stainless steel wire mesh. Hence, the current research at TAMU uses a copper mesh donut for the elastic support in a foil bearing.

Knowledge of the physical parameters affecting the viscous damping and stiffness of a metal mesh damper is paramount for its engineered design and scalability. Al-Khateeb [2] finds that dry friction and at least one more source of damping, possibly material hysteresis, influence the overall viscous damping of a metal mesh donut damper. Dynamic load tests on a metal mesh damper demonstrate frequency – amplitude dependent stiffness and equivalent viscous damping coefficients, i.e., a nonlinear forced performance. Choudhry and Vance [10] report design equations, empirically based, to predict stiffness and viscous damping coefficients of metal mesh donut dampers. The design equations, with stiffness and viscous damping coefficients as functions of metal mesh donut geometry and compactness ratio, rely on simple tests to identify the metal mesh effective Young's Modulus, at any specified excitation frequency.

Metal mesh dampers display nonlinear stiffness and viscous damping properties which makes their prediction difficult. Ertas and Luo [11] report characterizing the nonlinear stiffness and damping of metal mesh donuts by varying the vibration amplitude, excitation frequency, and static eccentricity. The tests show that the eccentricity (due to a static load) has no influence on the damper force coefficients. Also, maximum viscous damping is present at the lower frequency ranges (0-50 Hz) and viscous damping coefficient reduces from ~29 kNs/m (at 20 Hz) to ~3.5 kNs/m (at 300 Hz). The authors successfully demonstrate low rotor vibration levels through the first two critical speeds during high-speed tests with metal mesh donut as damping element.

Recently, Ertas [12] report a novel compliant hybrid journal bearing for enabling oil-free operation in high speed turbomachinery. The design integrates a flexurally supported multiple pad hybrid bearing and two metal mesh donuts, inserted under the pads at the bearing sides, maximizing load carrying capacity and effective damping without sacrificing compliance to misalignment between rotor and bearing. Test data show that the viscous damping decreases with increasing excitation frequency. The bearing direct stiffness decreases with increasing frequency with no external pressure applied into the bearing pads. But, with an applied feed pressure, the bearing direct stiffness shows an increasing trend with increasing frequency. Also, subsynchronous vibration components, present in rotordynamic tests without the dampers, are absent at the system natural frequency with the metal mesh dampers installed.

III. DESCRIPTION OF METAL MESH FOIL BEARING

III.1 METAL MESH FOIL BEARING COMPONENTS

Figure 2 shows a prototype of a constructed oil-free MMFB and Table 1 describes the three main components comprising a MMFB. The MMFBs use commercially available donut shaped metal mesh as the elastic support under the top foil. The top foil, a smooth arcuate surface 3 mil thick, is in contact with the shaft. In MMFBs, the metal mesh under the top foil also provides material damping and dry-friction energy dissipation effects [2].
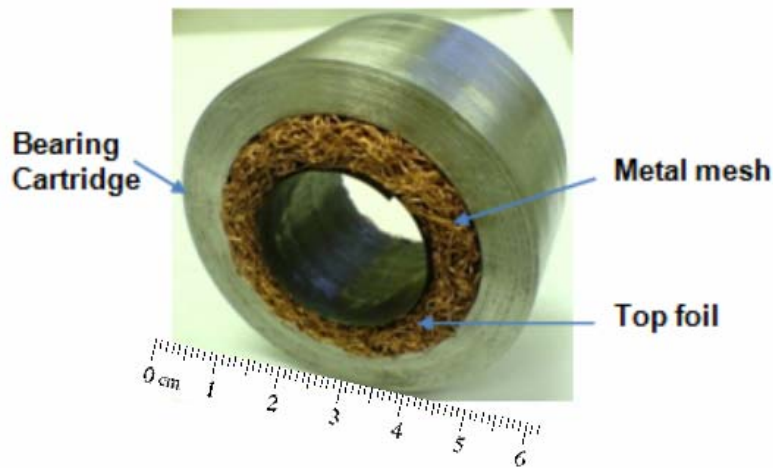
Figure 2. Photograph of a Metal Mesh Foil Bearing (MMFB) manufactured at TAMU

Table 1. Description of Metal Mesh Foil Bearing Components

	Description	Role
Bearing Cartridge	Stainless steel cylindrical ring	Cartridge holding metal mesh donut and smooth top foil.
Metal mesh donut (MM)	Donut shaped compressed woven wire mesh	Soft material support provides structural stiffness and energy dissipation
Smooth top Foil	Stainless steel sheet, curved and preformed, with one end affixed to the metal mesh donut and the other end free.	A hydrodynamic film pressure builds up within the gap between the rotating shaft and the top foil.

Figure 3 illustrates the installation of the top foil inside the metal mesh donut. The top foil has two identical shaped tabs at one end, which are bent and fit into the two apertures inside the donut shaped metal mesh during assembly, as shown in Figs. 3(a) and 3(b). After affixing the top foil into the metal mesh, the assembly is pushed into the bearing cartridge to complete the construction of the MMFB.
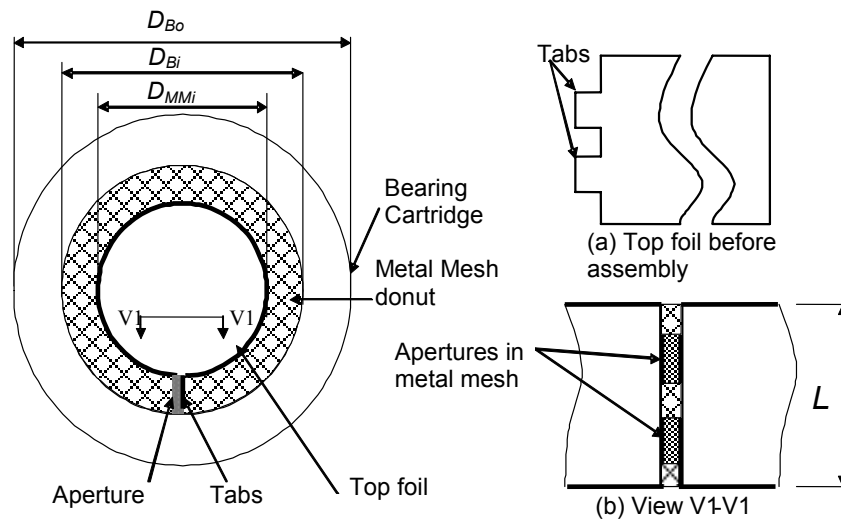
Figure 3. Schematic view of Metal Mesh Foil Bearing (MMFB), (a) View showing tabs at one end of top foil before assembly, (b) View showing two apertures in metal mesh donut

III.2 TEST MMFB GEOMETRY AND MATERIAL SPECIFICATIONS

The overall dimensions of the MMFB constructed follow that of gas foil bearings (GFBs) designed for use in automotive turbochargers. Ref [13], for example, details a patented GFB supported oil-free turbocharger. Table 2 shows the dimensions and material specifications for the constructed MMFB: a metal mesh donut with inner diameter of 28.30 mm and an axial length of 28.05 mm, a top foil thickness of 0.076 mm. The estimated bearing radial clearance is 0.03 mm with a mating shaft of 28.08 mm in diameter. The donut shaped MM has a wire diameter of 0.30 mm. The MM compactness (wire density) determines the physical (equivalent) properties [2].

Table 2. Nominal dimensions and material specifications for MMFB

Parameter name & physical dimension	Magnitude
Bearing cartridge outer diameter, D_{Bo} (mm)	58.15±0.02
Bearing cartridge inner diameter, D_{Bi} (mm)	42.10±0.02
Bearing axial length, L (mm)	28.05±0.02
Metal mesh outer diameter, D_{MMo} (mm)	42.10±0.02
Metal mesh inner diameter, D_{MMi} (mm)	28.30±0.02
Wire diameter, D_W (mm)**	0.30
Metal mesh mass, M_m (kg)	0.0391 ± 0.0001
Metal mesh density, ρ_{MM} (%)*	20
Top foil thickness, T_{tf} (mm)** (stainless steel)	0.076
Nominal radial clearance (μm)***	35
Copper Young modulus , E (GPa), at 21 ºC [14]	110
Copper Poisson ratio, υ [15]	0.34
Bearing mass (cartridge + mesh + top foil), M (kg)	**0.316 ± 0.0001**

* The density of metal mesh is defined by the manufacturer as the ratio of the donut mass to its volume divided by the material density. Metal mesh donut donated by Kinetic Structures Corp., http://www.kineticstructures.net.
** Nominal value provided by manufacturer.
*** Nominal value for a journal diameter D_J = 28.08 mm.

IV. EXPERIMENTAL DETERMINATION OF MMFB STATIC STRUCTURAL STIFFNESS

IV.1 STATIC LOAD TEST SETUP AND EXPERIMENTAL PROCEDURE

A series of static load – bearing deflection tests aid to estimate the static load performance of the constructed MMFB. The tests are conducted at room temperature. Figure 4 shows a schematic representation of the static load test setup with a MMFB supported on a shaft affixed in a lathe chuck. An eddy current sensor (ECS) with a sensitivity 8.24V/mm (209 mV/mil)[1] measures horizontal displacements *(X)* of the bearing, and a strain gauge type load cell, with sensitivity 0.225 V/N (0.1V/lb) measures the static load. One end of the load cell is threaded directly to the bearing mid-span, and the other end to a cylindrical steel rod affixed in a lathe tool holder. The forward and backward motions of the lathe tool holder transmit, through the load cell, push and pull loads to the bearing cartridge.

---

[1] Appendix B reports static displacement measurements on the bearing cartridge to determine the ECS gain.
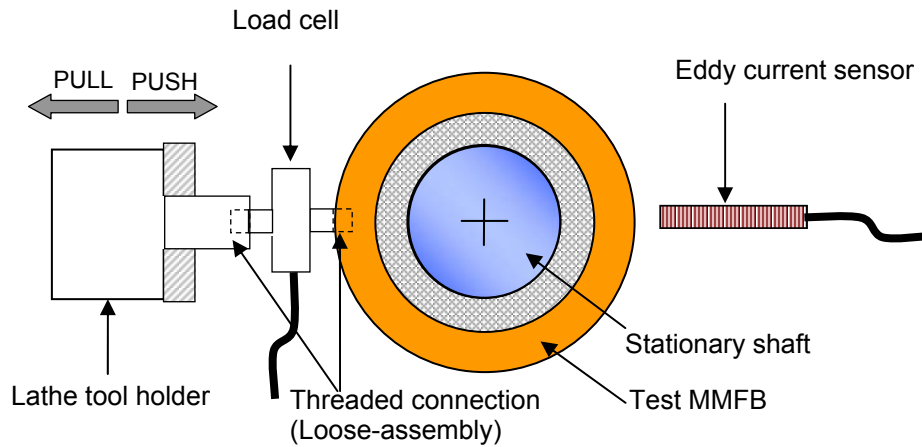
Figure 4. Schematic representation of the MMFB static load test setup

Three cycles of push and pull loads *(F)* are applied to the MMFB and displacements *(X)* are measured. The test data, modeled as a cubic polynomial in the displacement *(X),* provides a relation between the static load *(F)* and measured displacement *(X)*. The MMFB static stiffness coefficient *(K=$\frac{\partial F}{\partial X}$)* follows from differentiation of the polynomial found.

IV.2 EXPERIMENTAL RESULTS

Figure 5 shows the applied static load *(F)* versus measured MMFB displacement *(X)*. Markers and lines represent test data and their respective cubic polynomial curve fits. Note the hysteresis loop, representing mechanical energy dissipation, due to the nonlinear load versus deflection behavior of the MMFB during the push-pull loading tests. Note that the top foil, loosely installed inside the metal mesh donut and in contact with the mating shaft, causes an unknown MMFB geometric center, and thus the push load starts from an arbitrary offset displacement[2].

---

2   Test data in Fig. 5 is shifted by - 0.015 mm so that the center of the hysteresis loop coincides approximately with the origin of the displacement coordinate.
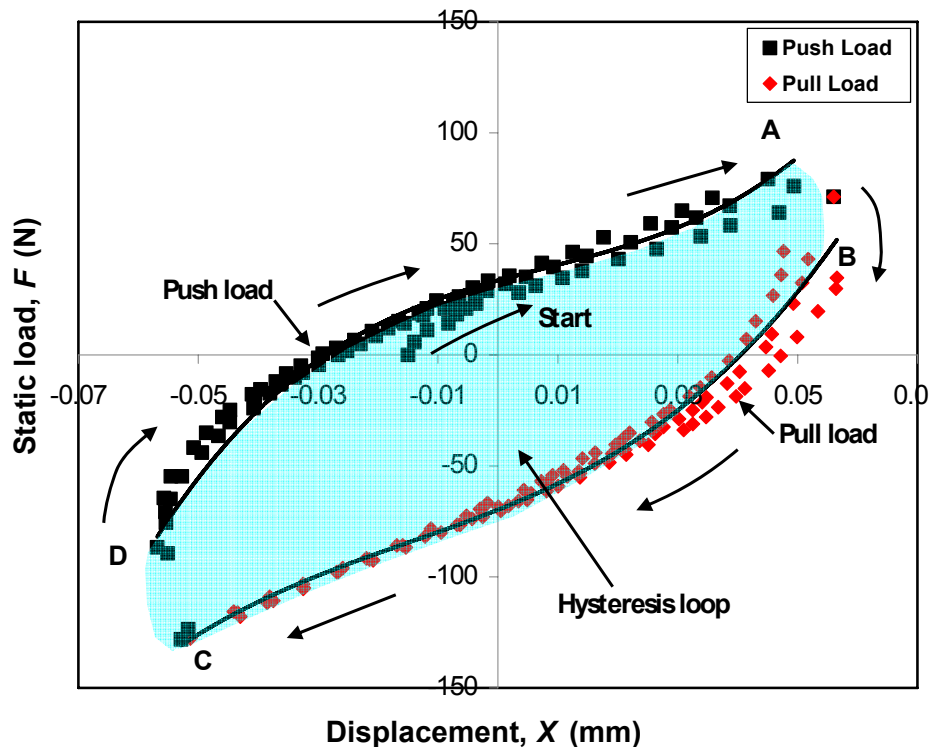
Figure 5. Applied static load versus measured MMFB displacement

Figure 6 shows the estimated MMFB structural stiffness *(K)* versus bearing static deflection *(X)*. Push and pull loads result in two different curves for the estimated stiffness coefficients of MMFB. Test starts with a no load *(F=0)* and continues in the forward direction till the maximum deflection point (A). Then, as the load reversal occurs, the stiffness instantaneously shifts to the point B and continues along the backward stiffness curve till point C. Again, as the loading reverses to the forward direction, the stiffness instantly builds up to point D. The sudden changes in stiffness at the points of load reversal are thought to be related to hysteresis and dry-friction effects of the metal mesh.
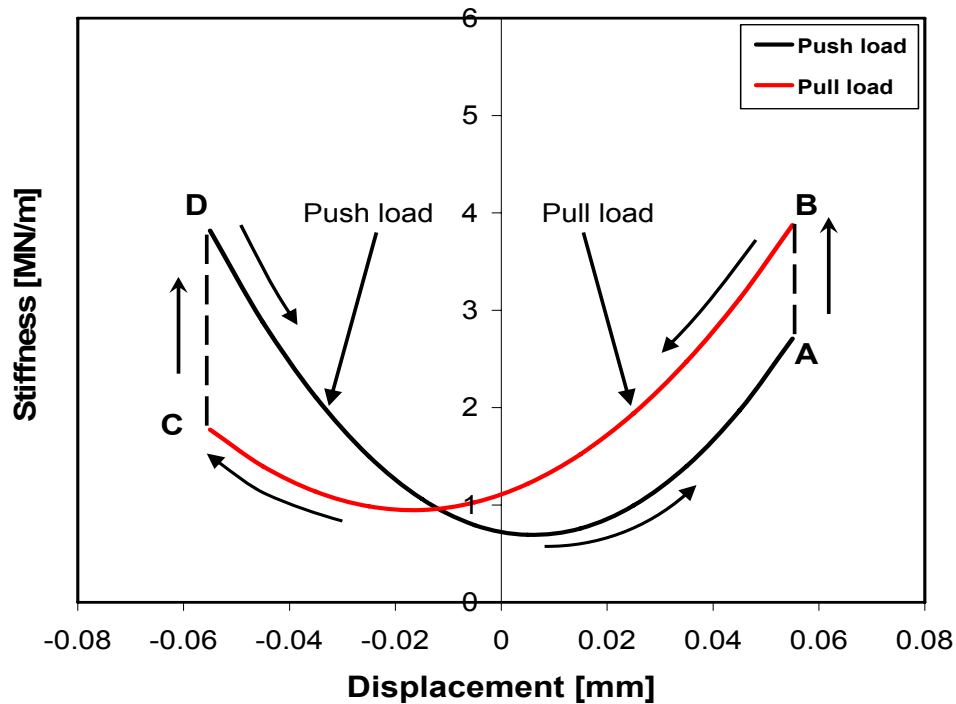
Figure 6. Estimated structural stiffness versus MMFB displacement

Tables 3 and 4 detail the coefficients of the cubic polynomials, goodness of fit, and estimated static structural stiffnesses for the test MMFB.

Table 3. MMFB static load versus deflection: coefficients of cubic curve fit

Loading direction	Load F [N] versus Deflection X [mm]	X Range [mm]	Correl-ation Factor[3]	Uncertainty[4] [N]
Push load	$F = 280104\,X^3 - 5039\,X^2 + 721.11\,X + 34.9$	[-0.06,0.06]	0.926	0.5
Pull load	$F = 189239\,X^3 + 9550.8\,X^2 + 1107.4\,X - 67.5$	[-0.06,0.06]	0.942	0.5

Table 4. Identified MMFB static structural stiffness versus deflection

Loading direction	Stiffness K [N/mm] versus Deflection X [mm]	X Range [mm]	Uncertainty [kN/m]
Push load	$K = 840312\,X^2 - 10078\,X + 721$	[-0.06,0.06]	4
Pull load	$K = 567717\,X^2 + 19101.6\,X + 1107$	[-0.06,0.06]	3

---

[3] The correlation factor indicates the goodness of the curve fit to the test data
[4] Uncertainty of the load cell (0.25% accuracy)

V. IDENTIFICATION OF MMFB DYNAMIC STRUCTURAL FORCE COEFFICIENTS

V.1 DYNAMIC LOAD TEST SETUP AND EXPERIMENTAL PROCEDURE

Dynamic load tests aid to identify the structural stiffness and equivalent viscous damping of the MMFB for increasing bearing displacements and excitation frequencies. Figure 7 shows a schematic representation of the setup for the dynamic load tests on the MMFB supported on a rigid shaft of diameter equal to 28.08 mm. A fixture, clamped to a rigid steel table, holds the shaft firmly. The fixture minimizes the motion between the shaft and the ground so that the bearing is the only component in motion during shaker testing[5]. The electromagnetic shaker, suspended with cables from the ceiling of the test facility, provides MMFB excitation forces along the horizontal direction for increasing excitation frequencies. An eddy current sensor measures the MMFB deflection. Ref. [16], identifying structural force coefficients of bump-type foil bearings, details the test setup and procedure.

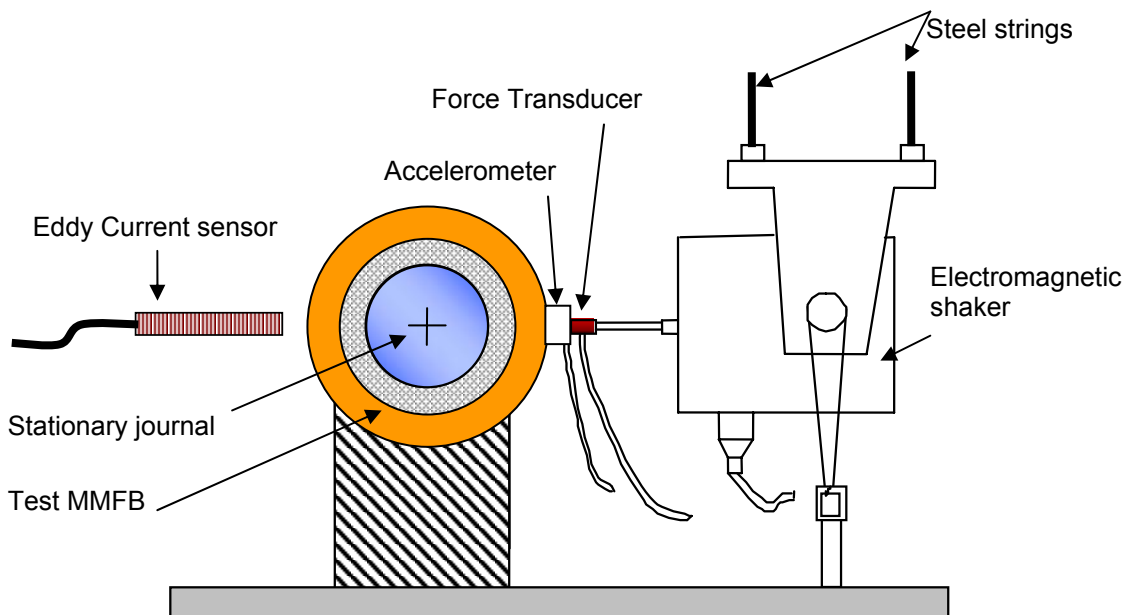
Figure 7. Schematic representation of the setup for dynamic load tests with the MMFB supported on a rigid shaft

---

[5] A separate eddy current sensor measures the shaft motions to be at most ~5% of MMFB displacements for the loads applied.

The load, displacement and acceleration are taken as inputs to the data acquisition system. Two eddy current sensors (sensitivity 8.24V/mm (209mV/mil)) measure the displacement of the bearing and the shaft, a piezoelectric accelerometer (sensitivity 5 mV/g), magnetically mounted on the bearing cartridge, measures the acceleration of the bearing cartridge, and a force transducer (sensitivity 11.2 mV/N), threaded directly to the bearing cartridge at its axial mid-span, measures the dynamic load acting on the MMFB.

The experiments for identification of MMFB structural force coefficients involve single frequency dynamic load excitations with three MMFB motion amplitudes (12.7 μm, 25.4 μm, 38.1 μm). The dynamic load is applied with frequency ranging from 25 to 400 Hz, varying at 25 Hz increments. All test cases are repeated twice.

A LabVIEW® in-house program controls inputs to the shaker, acquires outputs from sensors, and displays real-time test results. The user inputs the desired amplitude of dynamic displacement, and an algorithm tunes the voltage amplitude to the electromagnetic shaker to get the desired load.

V.2 EXPERIMENTAL RESULTS

A single degree of freedom mechanical system with constant parameters represents best the non-rotating test system [16]. The MMFB motion $x(t)$ due to an excitation force $f(t)$ is governed by

$$M\ddot{x}(t) + C\dot{x}(t) + K x(t) = f(t) \tag{1}$$

where $M=0.316$ kg is the metal mesh bearing mass, and C and K are the metal mesh bearing equivalent viscous damping and structural stiffness coefficients, respectively. For a single frequency (ω) force excitation $f(t) = \bar{F}e^{i\omega t}$, the bearing motion response is $x(t) = \bar{X}e^{i\omega t}$. Hence, Eq. (1) becomes in the frequency domain

$$\bar{F} = -M\omega^2 \bar{X} + i\omega C \bar{X} + K \bar{X} \tag{2}$$

Ready evaluation of the stiffness *(K)* and viscous damping *(C)* coefficients follow from the impedance function

$$Z = K + iC\omega = \frac{\overline{F}}{\overline{X}} + M\omega^2 \qquad (3)$$

Thus, $K = Re(Z)$ and $C = \dfrac{Im(Z)}{\omega}$. In addition, from simple vibration knowledge [17]

$$C\omega = \gamma K \qquad (4)$$

where, γ is a structural loss factor representing material damping.

Figure 8 shows a typical waterfall plot of the dynamic loads for excitation frequencies from 25 Hz to 400 Hz. The amplitude of dynamic load, $|\overline{F}|$ required to maintain constant bearing amplitude of motion, $|\overline{X}|$ decreases with increasing frequency.
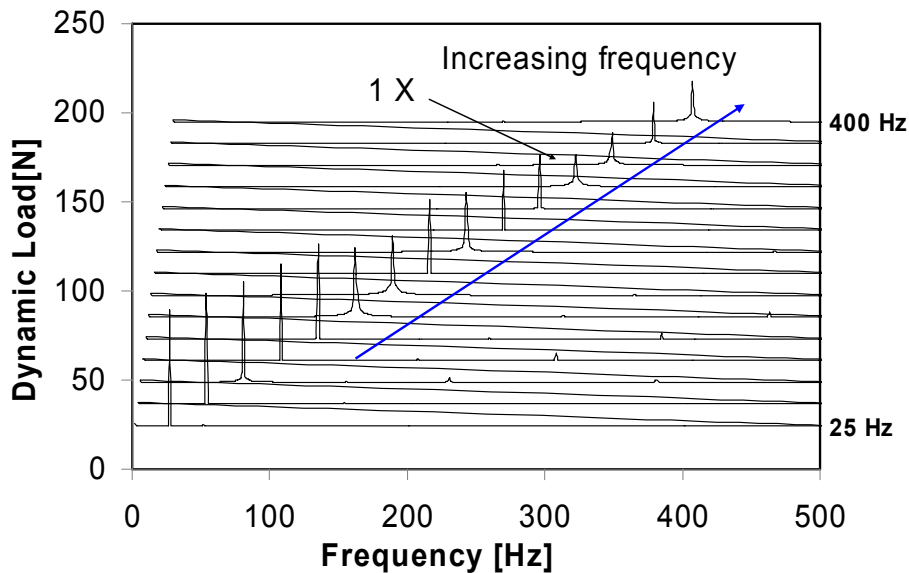

Figure 8. Waterfall plot of dynamic load for motion amplitude of 38.1 μm and excitation frequencies from 25 to 400 Hz

Figure 9 shows a typical waterfall plot of the MMFB dynamic displacement response to forced excitations with frequency ranging from 25 Hz to 400 Hz. The shaker is controlled to produce a constant MMFB motion amplitude of 38.1 μm (0 - pk.) over the whole frequency

range. The graph shows dominant MMFB motion amplitudes (1X) synchronous to the excitation frequency. Motion amplitudes in other harmonics are negligibly small.
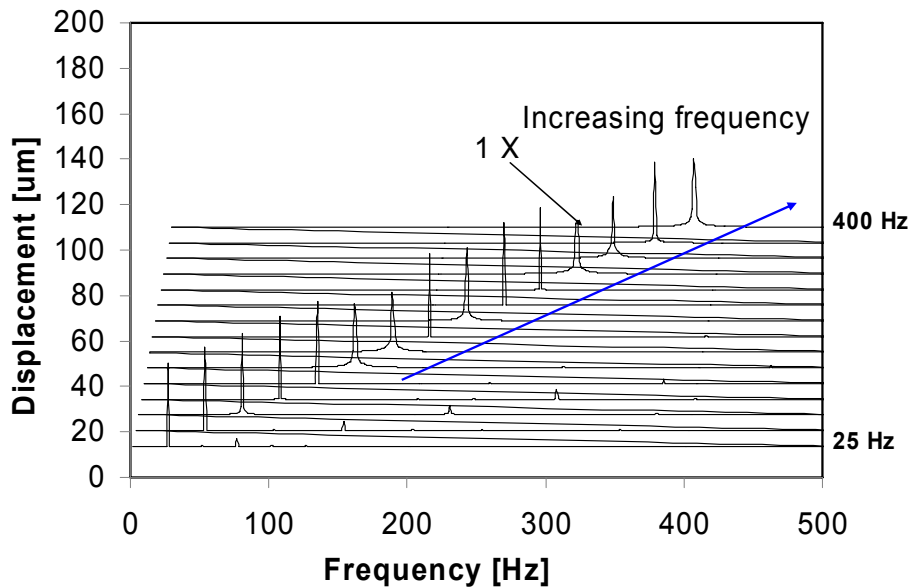
Figure 9. Waterfall plot of bearing displacement for motion amplitude of 38.1 μm and excitation frequencies from 25 to 400 Hz

Figure 10 shows the variation of dynamic load amplitudes generating three constant MMFB motion amplitudes (12.7 μm, 25.4 μm, 38.1 μm) versus frequency. The amplitude of dynamic load decreases as the displacement amplitude decreases and as the excitation frequency increases. The maximum difference between input loads for a first and a second test is 24 % and occurs at the lowest excitation frequency of 25Hz. Above 100 Hz, the differences are less than 15%.
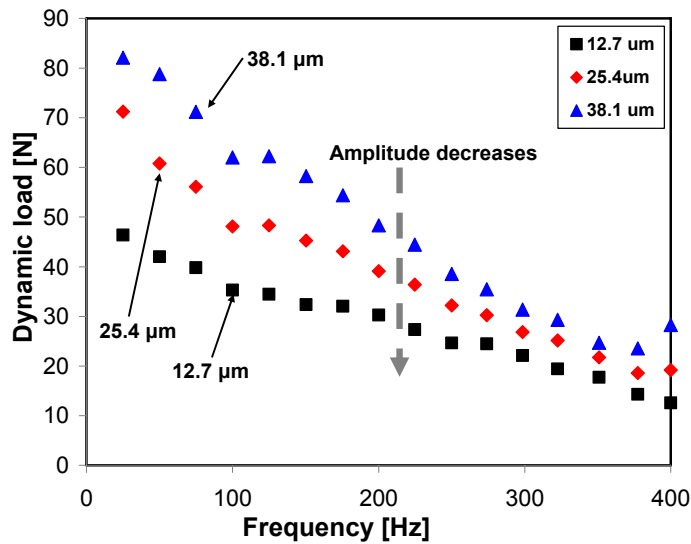
(a) Test 1
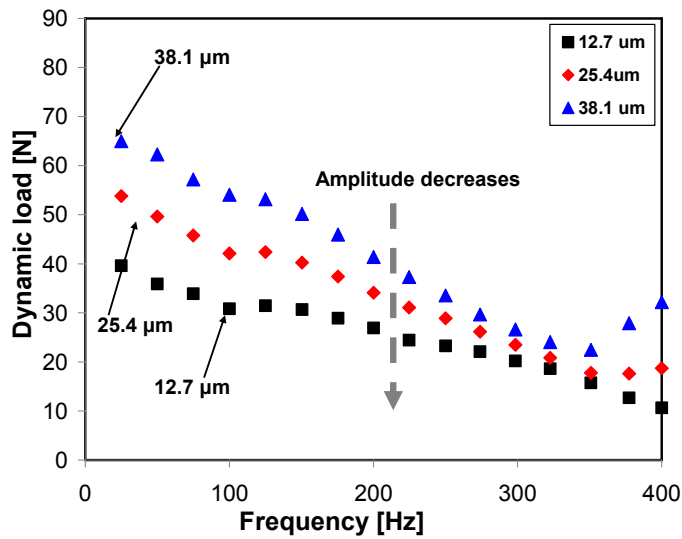
(b) Test 2

Figure 10. Amplitude of load acting on the MMFB versus frequency of excitation for three motion amplitudes (12.7 μm, 25.4 μm, 38.1 μm). (a)Test 1, (b) Test 2

Figure 11 shows the real part of $(\bar{F} / \bar{X})$ versus frequency for two dynamic load tests. The system dynamic stiffness decreases with either an increase in excitation frequency or an increase in amplitude of motion.
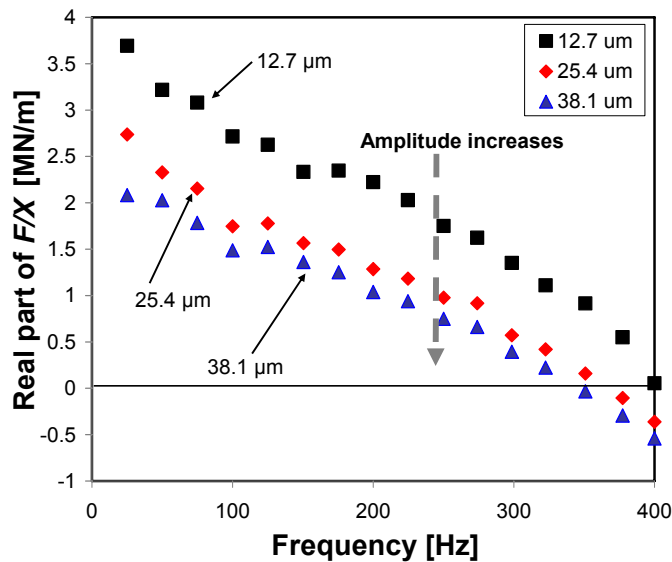
(a)Test 1
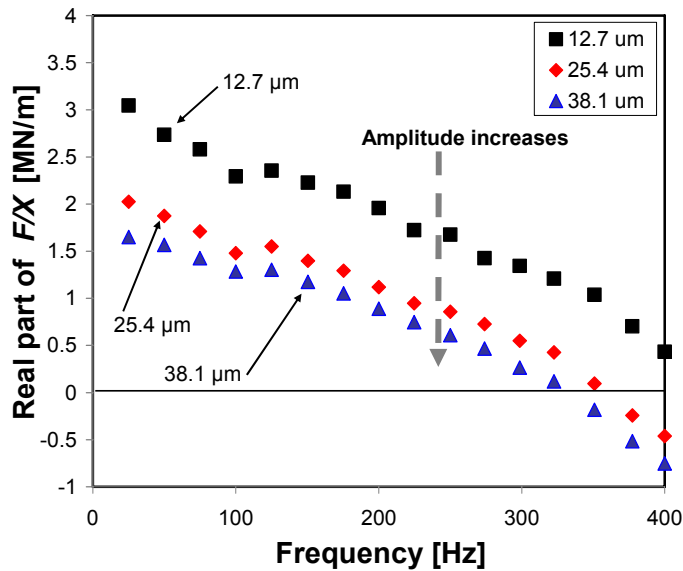
(b)Test 2

Figure 11. Real part of $(\bar{F} / \bar{X})$ - dynamic stiffness- versus frequency of excitation derived from three motion amplitudes (12.7 μm, 25.4 μm, 38.1 μm). (a) Test 1, (b) Test 2

Figure 12 shows the MMFB structural stiffness *(K)* versus frequency identified from two tests. The bearing structural stiffness decreases with increasing motion amplitudes. In the range of low to moderate frequencies (25 Hz - 100 Hz), the stiffness *K* decreases rapidly (~25 %). For larger frequencies, *K* continues to decrease, but more gradually.

Al-Khateeb [2] introduces a stick slip model to explain metal mesh stiffness behavior. The stick-slip model arranges the metal wires in the metal mesh donut in a series combination of hysteretic dampers and linear springs. At a particular frequency, with an increase in applied force, more stick-slip joints between the metal wires overcome friction forces and become free. These increased spring damper layers cause a reduction of stiffness of the metal mesh donut. Ertas and Luo [11] also report a similar trend for structural stiffness of a metal mesh damper in forced load excitation tests.

Figure 13 shows the quadrature stiffness of $(\bar{F}/\bar{X})$ decreases with an increase in displacement amplitude, while appearing nearly frequency independent. The test data shows that the energy dissipation mechanism is not of viscous type. Otherwise, the data will follow a straight line whose slope represents the viscous damping coefficient, i.e. $\sim C\omega$.

Figure 14 shows the estimated structural loss factor (γ) versus frequency of excitation for two dynamic load tests conducted on the MMFB. The structural loss factor (γ), albeit increasing slightly from 25 Hz to 150Hz, is nearly frequency independent at the highest frequencies of excitation ($\sim$400 Hz). The identification shows a loss factor as high as 0.50, a significant magnitude for the simple mechanical system.

Figures 15 and 16 present the MMFB structural stiffness (K) and equivalent viscous damping (C) versus motion amplitude, respectively, for increasing excitation frequencies. Note the logarithmic scale for the vertical axis in Fig.16. The K and C magnitudes derived from a simple average of the two dynamic load test values show that the MMFB structural stiffness (K) and equivalent viscous damping (C) decrease nonlinearly with increasing amplitudes of motion.

The uncertainties of the estimated structural force coefficients (stiffness and damping) are yet to be determined. Incidentally, the variability of the identified parameters also needs careful assessment.
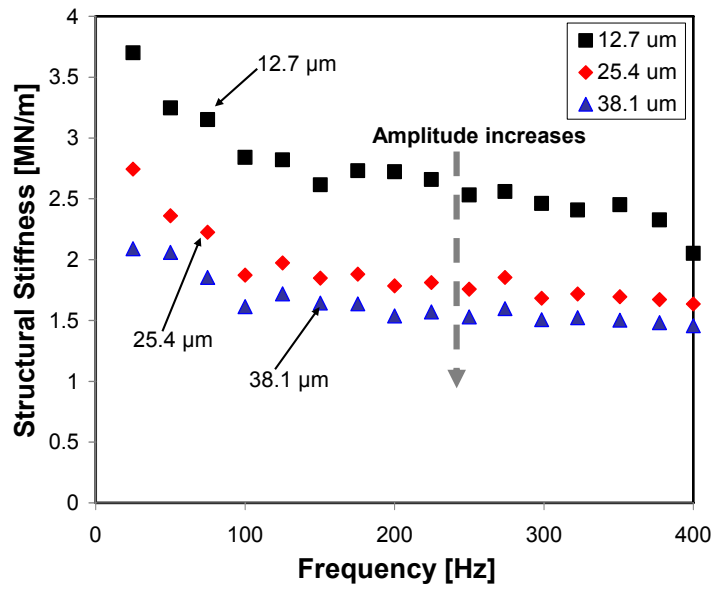
(a) Test 1
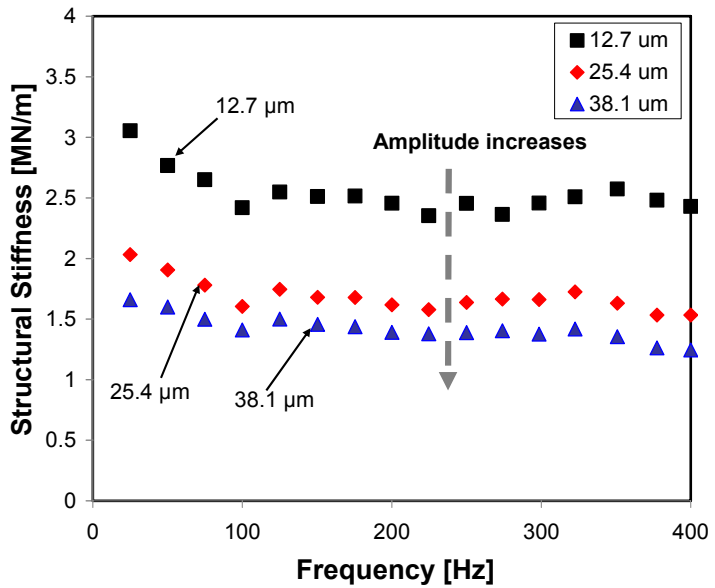
(b) Test 2

Figure 12. MMFB structural stiffness *(K)* versus frequency derived from three motion amplitudes (12.7 μm, 25.4 μm, 38.1 μm). (a)Test 1, (b) Test 2
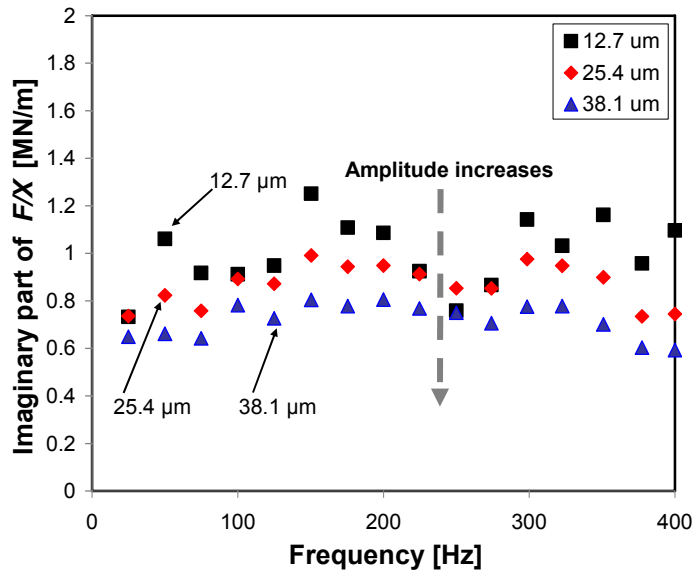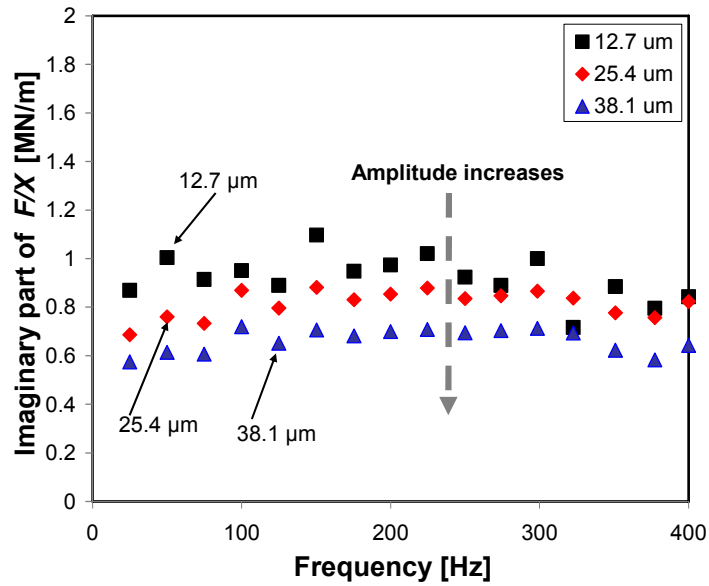
(a) Test 1

(b) Test 2

Figure 13. Imaginary part of $(\bar{F}/\bar{X})$ - quadrature stiffness- versus frequency of excitation derived from three motion amplitudes (12.7 μm, 25.4 μm, 38.1 μm). (a) Test 1, (b) Test 2
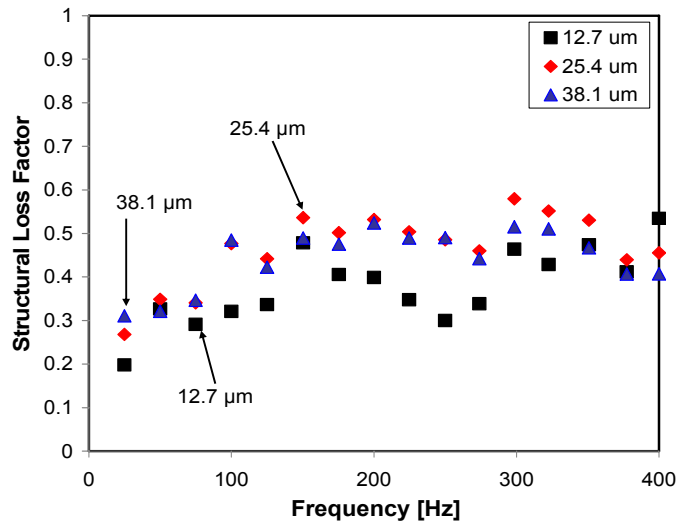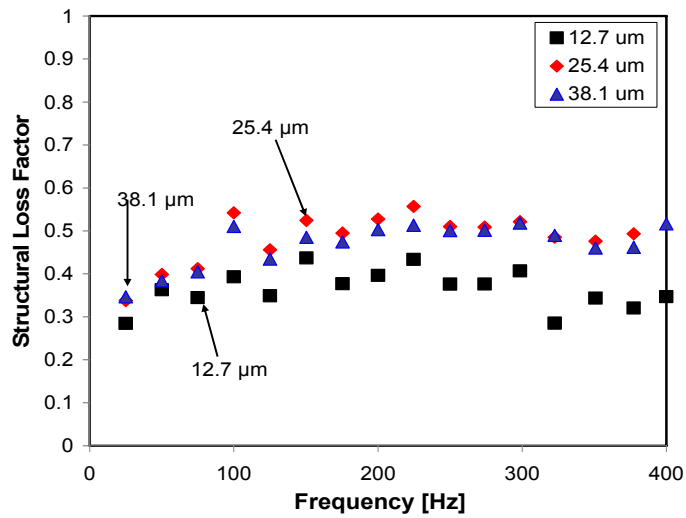
(a) Test 1

(b) Test 2

Figure 14. Structural loss factor (γ) versus frequency of excitation derived from three motion amplitudes (12.7 μm, 25.4 μm, 38.1 μm). (a) Test 1, (b) Test 2

Figure 15. MMFB structural stiffness *(K)* versus motion amplitude for increasing excitation frequencies. Mean values of tests 1 & 2 data

Figure 16. MMFB equivalent viscous damping *(C)* versus motion amplitude for increasing excitation frequencies. Mean values of tests 1 & 2 data

VI. MODEL PREDICTIONS COMPARED TO IDENTIFIED FORCE COEFFICIENTS

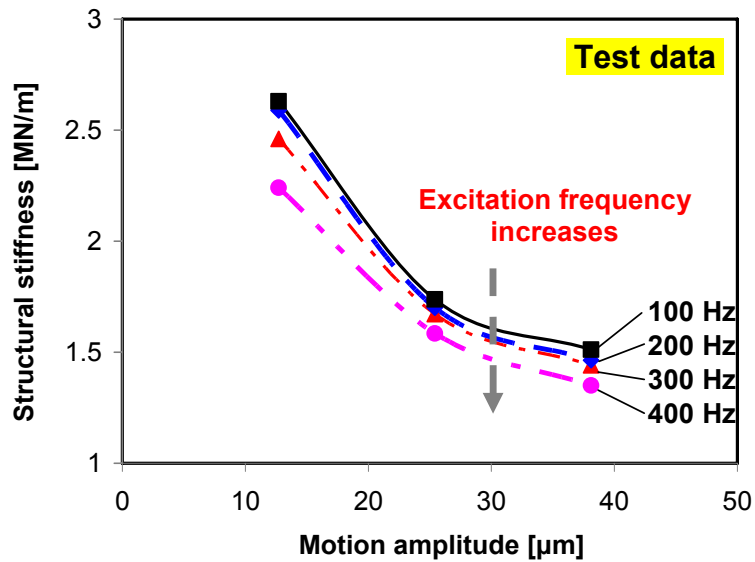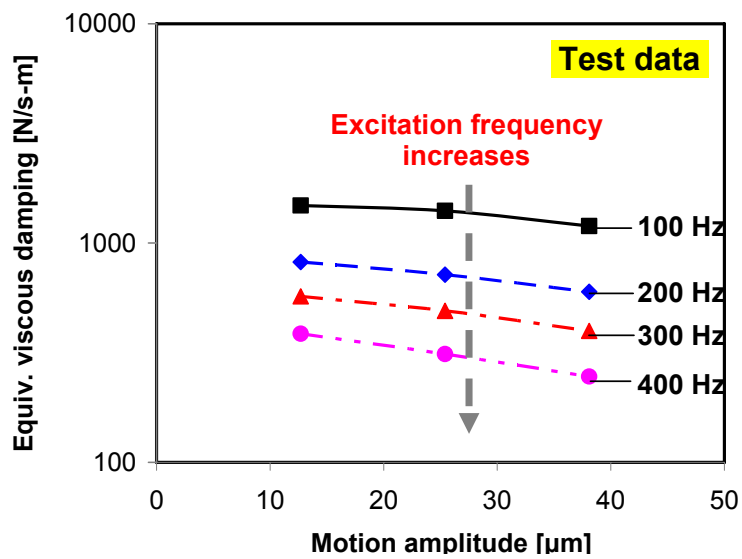Predictions of structural stiffness and damping coefficient for the MMFB use empirical equations in Ref. [10]. These formulas are derived from structural dynamic load test data obtained with four metal mesh dampers (MMDs) of various radial thicknesses. In Ref. [10], dynamic load tests quantify the effects of axial compression, radial interference, and motion amplitude on the stiffness and damping coefficients of the tested metal mesh dampers. These MMDs have a wire diameter (D_W) of 0.32 mm and a density (ρ_{MM}) of 42.7 %. Reference [2] provides further test data for metal mesh donut force coefficients for increasing excitation frequencies and extends the predictive equation to include the effects of frequency.

Thus, Eqs. (5-8) below, taken from Ref. [10], predict metal mesh stiffness (K) and viscous damping (C) coefficients as functions of an equivalent modulus of elasticity (E_{equiv}), material hysteresis damping coefficient (H_{equiv}), axial length (L), inner radius (R_i), outer radius (R_o), axial compression ratio (C_A), radial interference (R_p), motion amplitude (A), and excitation frequency (ω) [2], i.e.,

$$K = E_{equiv} \cdot f\left(L, R_o, R_i\right) \cdot f\left(C_A\right) \cdot f\left(R_p\right) \cdot f\left(A\right) \cdot f\left(\omega\right) \tag{5}$$

$$C = H_{equiv} \cdot g\left(L, R_o, R_i\right) \cdot g\left(C_A\right) \cdot g\left(R_p\right) \cdot g\left(A\right) \cdot g\left(\omega\right) \tag{6}$$

where

$$K = E_{equiv} \cdot \frac{L}{\left(R_o - R_i\right)} \cdot \left[1 + 4 \cdot 10^{-5}\left(\frac{C_A}{L}\right)^2\right] \cdot \left[1 + 2.96 \cdot 10^{-2}\left(\frac{R_p}{R_o - R_i}\right)\right] \cdot \left[1 + \tilde{C}_{K_1}\left(\frac{A}{R_o - R_i}\right)^{-2/3}\right] \cdot \left[\tilde{C}_{K_1}{}^{\omega}\right] \tag{7}$$

and

$$C = H_{equiv} \cdot \frac{L}{\left(R_o - R_i\right)} \cdot \left[1 + 8.7 \cdot 10^{-5}\left(\frac{C_A}{L}\right)^2\right] \cdot \left[1 + 1.8 \cdot 10^{-2}\left(\frac{R_p}{R_o - R_i}\right)^{3/2}\right] \cdot \left[1 + \tilde{C}_{C_1}\left(\frac{A}{R_o - R_i}\right)^{-2/3}\right] \cdot \left[\left(\frac{\omega}{\omega_n}\right)^{\tilde{C}_{C_2}}\right] \tag{8}$$

with $\tilde{C}_{K_1} = 3.92$, $\tilde{C}_{K_1} = 0.9999$, $\tilde{C}_{C_1} = 2.59$, and $\tilde{C}_{C_2} = $ -0.16.

TRC-B&C-5-08

Table 5 lists the parameters for prediction of the structural stiffness and viscous damping coefficients of the MMFB tested.

Table 5. Parameters of test metal mesh donut for evaluation of stiffness and damping

Parameter name and physical dimension	Value
Metal mesh axial length, L (mm)	28.05
Metal mesh outer radius, $R_o = D_{MMo}/2$ (mm)	21.05
Metal mesh inner diameter, $R_i = D_{MMi}/2$ (mm)	14.04
Axial compression, C_A (mm)	0.0
Radial interference, R_p (mm)	0.0
Max. amplitude, A (µm)	12.7, 25.4, 38.1
Excitation frequency, ω (Hz)	25 – 400
Equivalent modulus of elasticity, E_{equiv} (N/m)[6]	7.9×10^6
Equivalent hysteresis damping parameter, H_{equiv} (Ns/m)	8.4×10^4

Figure 17 depicts the predicted MMFB structural stiffness (K) versus excitation frequency for increasing motion amplitudes. The predicted and test identified stiffness, shown in Figure 12, decrease as both the excitation frequency and motion amplitude increase. Figure 18 shows the predicted MMFB equivalent viscous damping (C) versus excitation frequency for increasing motion amplitudes. Note the log scale for the vertical axis. The predicted equivalent viscous damping coefficient decreases as the excitation frequency increases and as the amplitude of motion increases. The experimental viscous damping coefficient, derived from the imaginary part of the mechanical impedance, decreases with increasing motion amplitudes, see Figure 13. In general, the predictions show excellent agreement with test data, thus validating equations (5-8).

---

[6]The current test MMFB has smaller wire diameter ($D_{W_{present}}$ = 0.3 mm) and density ($\rho_{MM_{present}}$ =20%) than those tested earlier [10], i.e., $D_{W_{past}}$ = 0.32 mm and $\rho_{MM_{past}}$ = 42.7 %. Presently the equivalent modulus of elasticity (E_{equiv}) and hysteresis damping coefficient (H_{equiv}) are estimated from the assumption that $E_{equiv} \propto \left(\rho_{MM_{present}} / \rho_{MM_{past}} \right)^3$ and $H_{equiv} \propto \left(\rho_{MM_{present}} / \rho_{MM_{past}} \right)$.
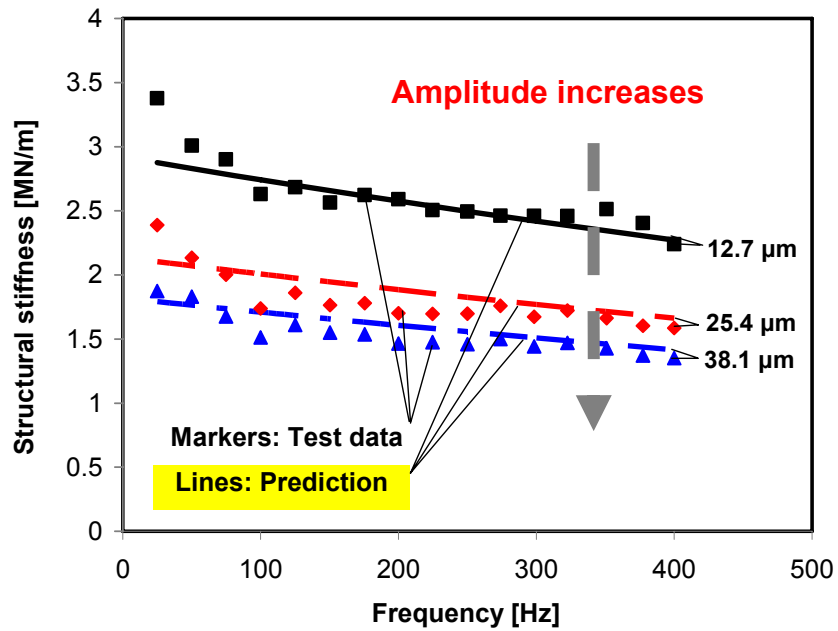
Figure 17. MMFB structural stiffness *(K)* **versus excitation frequency for increasing motion amplitudes (12.7 µm, 25.4 µm, 38.1 µm). Model predictions compared to mean values of test data [Fig. 12 (a,b)]**

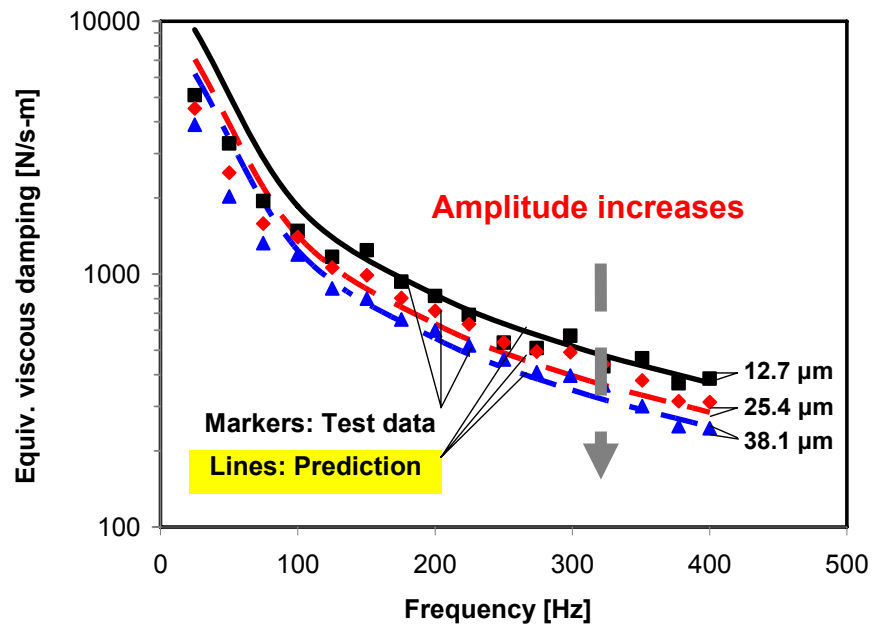**Figure 18. MMFB equivalent viscous damping (***C***) versus excitation frequency for increasing motion amplitudes (12.7 µm, 25.4 µm, 38.1 µm). Model predictions compared to mean values of test data [Fig. 13 (a,b)]**

VII. CONSTRUCTION OF AIR (TC) TURBINE DRIVEN TEST RIG AND PLANNED TESTS

A new test rig is under construction to evaluate the rotordynamic performance of MMFBs for operation under a specific static load and over a range of rotor speeds. The test rig comprises of an air turbine(TC)[7] driving an over-hung shaft stub and journal, a squirrel cage supporting a test bearing, and a linear positioning table and instrumentation for measuring rotor speed, bearing load and bearing displacements. Figure 19 shows the current configuration of the turbocharger driven MMFB test rig. The shaft stub is 5mm in diameter and 35 mm in length, and the journal is 28 mm in outer diameter. The journal is press fitted on the TC shaft stub and secured in place using a shaft nut. The journal has eight equally spaced threaded holes on its front face to insert weights for in-place dynamic balancing. A compressor facility can deliver air to a maximum of 18.2 bar (250 psig) and maximum 42.5 m³/min (1,500 SCFM). A pressure regulator, 9.30 bar (120 psig) max., adjusts the inlet pressure into the turbine. A ball valve throttles the inlet air to the turbine and the exhaust air is routed to the outside of the test cell. The turbine and journal system, with no bearing in place, achieved a speed of 110 krpm with a supply pressure of 5.51 bar (80 psig). The maximum rotational speed is expected to be ~ 120 krpm.

An infrared tachometer, mounted within the safety structure, measures the turbine tip speed with ± 0.0015 % accuracy. Figure 20 shows a schematic representation of the air turbine driven test rig. The right side view (a) shows the force transducer connected to the torque arm, squirrel cage, hollow journal and a positioning table. The front view (b) shows the static loading device with pulleys and weights. The torque measuring device is similar to that reported in Ref. [18].

---

[7] Twin ball bearing turbocharger- model T25, donated by Honeywell Turbo Technologies
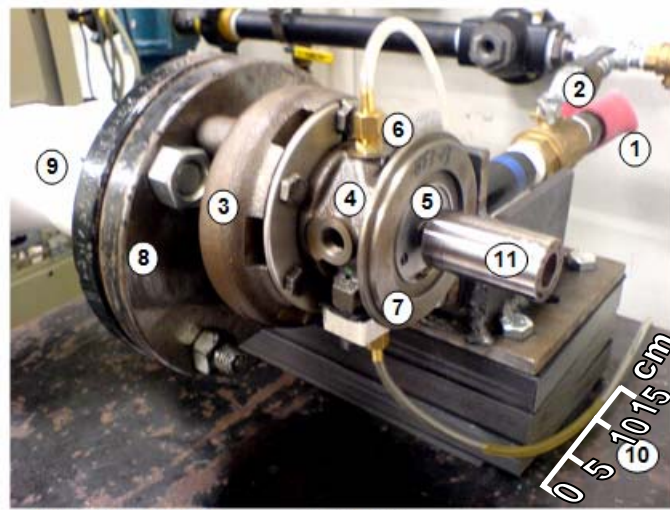
1. 9.30 bar Air Supply
2. Throttle Valve
3. Turbine Housing
4. Center Housing
5. Stub Shaft
6. Oil Inlet
7. Oil Outlet
8. Turbine Outlet Safety structure
9. Turbine exhaust
10. ¾" Thick Steel Tabletop
11. Test journal (28mm outer diameter hollow shaft)

Figure 19. Photograph of air turbine driven gas foil bearing test rig (Current configuration)

(a) Right side view
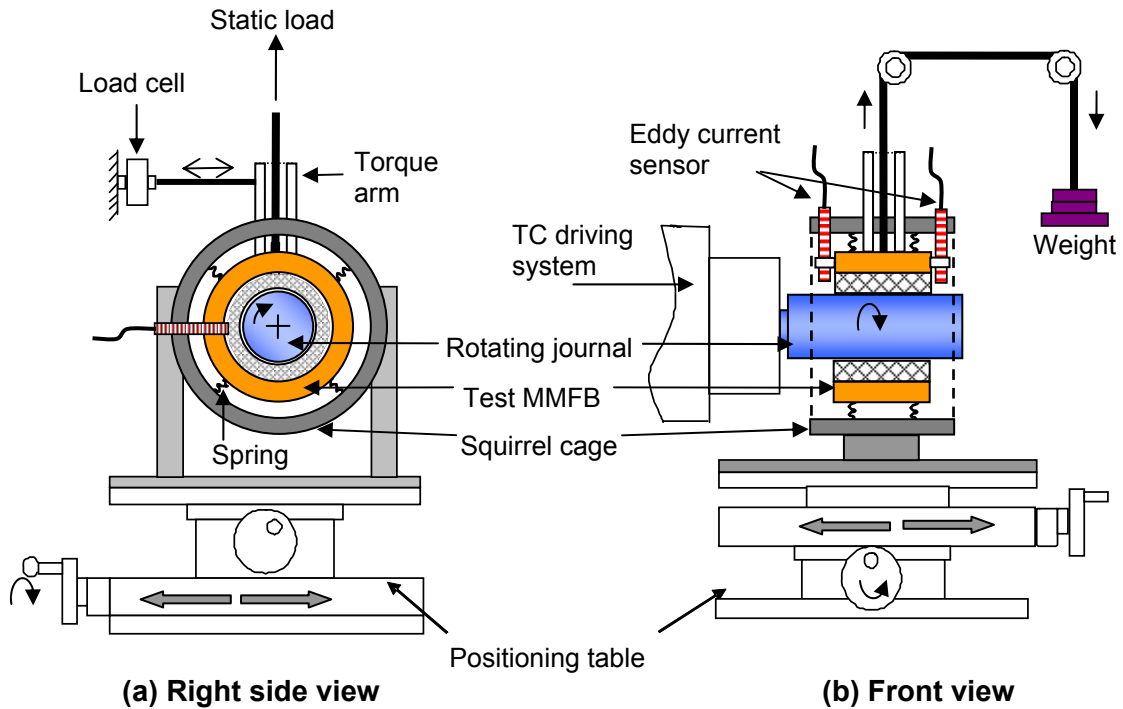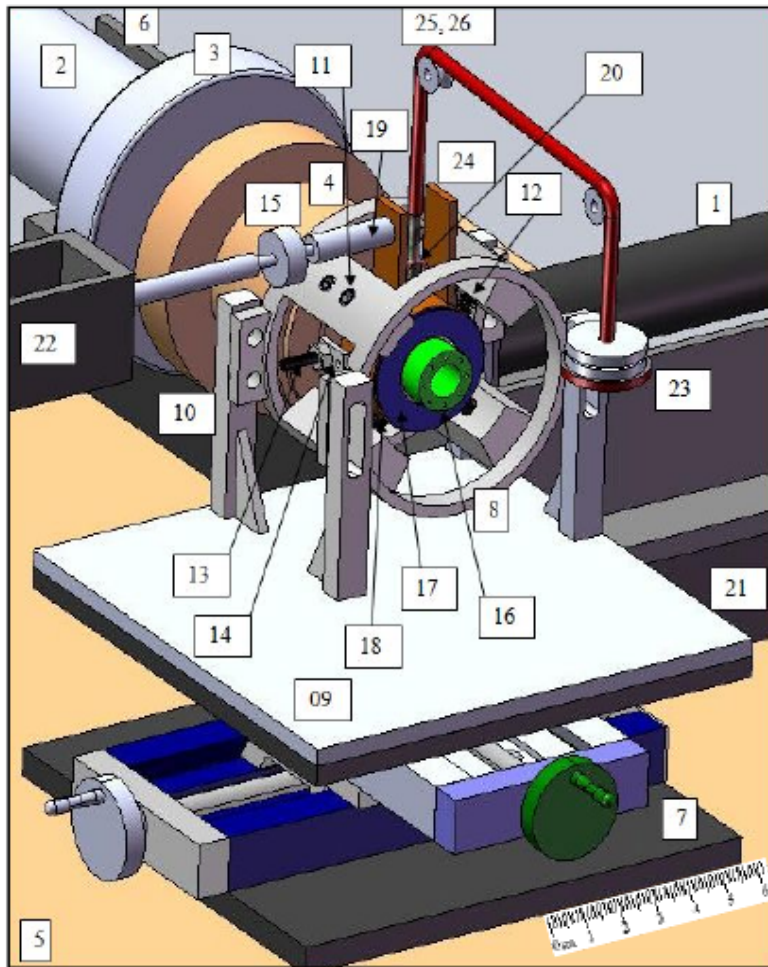
(b) Front view

Figure 20. Schematic views of turbine driven gas bearing test rig

Figure 21 shows a 3D CAD model of the test rig consisting of a turbine driven shaft stub (not visible), journal, Metal Mesh Foil Bearing, loading device, positioning table, squirrel cage and instruments for measuring bearing displacement and load. A positioning table, max, weight of 110N, offers a 3" x 3" travel distance along two horizontal coordinates, with a resolution of ±1 μm. The mechanism allows accurate positioning of the squirrel cage.

The squirrel cage (8) is affixed to a linear positioning table (7) using a base plate (9) and four vertical support plates (10). The slots on the vertical support plates allow adjusting the position of the squirrel cage in the vertical direction. The squirrel cage is bolted to the vertical support plates at the desired position. Eight compression springs provide soft connections between the squirrel cage and the test bearing. Dead weights apply upward increasing static loads on the test bearing using flexible string (25) and pulleys (26).

Four eddy current sensors measure displacements of the journal relative to the test bearing in the vertical and horizontal directions at two planes near the journal edges. A strain gauge type load cell, accuracy of ± 0.25%, is attached to the torque arm mounted on the bearing cartridge to measure the bearing drag torque during shaft rotation. Appendix D presents the dynamic characterization of the TC driven MMFB test rig.

1. Air supply
2. Exhaust
3. Turbine outlet safety structure
4. Turbine
5. Steel table
6. Turbine support structure
7. XY positioning table
8. Squirrel Cage
9. Squirrel Cage base plate
10. Squirrel Cage vertical support plate
11. Grub screw
12. Spring
13. Position sensing probe
14. Probe support plate
15. Force transducer
16. Test Journal
17. Test Journal end plate
18. Metal mesh foil bearing
19. Torque socket
20. Eye bolt
21. TC support structure block
22. Load cell support
23. Weights
24. Torque Arm
25. Loading string
26. Pulley

Figure 21. 3D CAD drawing of TC driven Metal Mesh Foil bearing test rig with instrumentation

The following tests on the metal mesh foil bearing test rig are planned for 2008-09:

a) Static load deflection tests with small displacement loops

Static load deflection tests, conducted with small displacements around various specified static loads aim to identify structural loss factors. The area enclosed by the hysteresis loop indicates the energy dissipated during the load-deflection cycle.

b) Bearing torque measurements

Bearing torque, while the journal contacts the bearing, is due to friction forces and contact pressures between the journal and top foil. Contact stress occurs due to external applied loads and the spring preloading of the foil against the shaft. The MMFBs will be lightly preloaded using springs installed in the squirrel cage to maintain shaft concentricity.

c) Load capacity tests

Load capacity is defined as the maximum load that is supported by a bearing operating with constant speed and 'steady state conditions'. Incrementally advancing the static load and rotor speed, a state is reached when the hydrodynamic film starts to rupture. This is observed by a sharp rise in bearing torque. The static load corresponds to the load capacity of the bearing at this speed. A relation between load capacity and speed for a bearing is obtained by controlled variation of operating speed and observing the rupture of the hydrodynamic film.

d) Rotor speed up and coast down tests

A rotor speed-up (acceleration) test determines the threshold speed of instability at the start of the abrupt rise of (any) sub synchronous motion. Imbalance response measurements conducted during rotor speed coast downs.

VIII. CLOSURE

Metal mesh, a compressed weave of metal wires, is sought as a cost effective replacement for the elastic support structure in gas bearings. A Metal Mesh Foil Bearing (MMFB) is assembled using a donut shaped metal mesh, a formed and annealed top foil, and a bearing cartridge. The MMFB, 28.15 mm in diameter and 28.05 mm in length, is made of 0.3 mm Copper wire with a compactness of 20 %. Static load versus bearing deflection measurements show a nonlinear load-deflection relationship with a large hysteresis, indicating large mechanical energy dissipation. Dynamic load tests aid to the estimation of the bearing mechanical impedance, whose real and imaginary parts determine the bearing structural stiffness and structural loss factor respectively. The bearing stiffness decreases with either an increase in frequency or an increase in amplitude of motion. The identified loss factor is as high as 0.50, a large magnitude for the simple bearing configuration, and shows little dependency on the excitation frequency. Predicted bearing force coefficients, based on published metal mesh damper design equations are in good agreement with the experimental mean values.

The report also details the current configuration of a turbocharger (TC) driven test rig for evaluating the rotordynamic performance of gas bearings. The bearing is supported on a journal that is press fitted onto the TC shaft stub. A centering elastic support, mounted on a two axes positioning table, holds the bearing cartridge softly. A pressure regulator, 9.3 bar (120 psig) max., adjusts the inlet pressure into the turbine. The turbocharger drive system, with an expected maximum rotational speed of 120 krpm, achieved a speed of 110 krpm with a supply pressure of 5.5 bar (80 psig). The test rig will be capable of measuring the bearing torque, bearing displacements and shaft speed.

IX. REFERENCES

[1] Agrawal, G., 1997, "Foil Air/Gas Bearing Technology – an Overview," ASME Paper No. 97-GT-347.

[2] Al-Khateeb, E. M., 2002, "Design, Modeling and Experimental Investigation of Wire Mesh Vibration Dampers," PhD. Thesis, Texas A&M University.

[3] Lee, Y. B., Kim, C. H., Jo, J. H., and Ryun, K., 2006, "Air Foil Bearing Having a Porous Foil, " International Patent No. WO 2006/043736 A1.

[4] Zarzour, M. J., 1999, "Experimental Evaluation of a Metal-Mesh Bearing Damper in a High Speed Test Rig," M.S. Thesis, Texas A&M University.

[5] Commercial Application of Metal Meshes, http://www.kineticstructures.net, accessed Apr. 23, 2008.

[6] Okayasu, A., Ohta, T., Azuma, T., Fujita, T., and Aoki, H., 1990, "Vibration Problems in the LE-7 Liquid Hydrogen Turbopump," AIAA Paper No. AIAA-1990-2250

[7] Al-Khateeb, E. M., and Vance, J. M., 2001, "Experimental Evaluation of a Metal Mesh Bearing Damper in Parallel with a Structural Support," ASME Paper No. 2001-GT-0247.

[8] Ertas, B. H., Al-Khateeb, E. M., and Vance, J. M., 2003, "Rotordynamic Bearing Dampers for Cryogenic Rocket Engine Turbopumps, " AIAA J. Propul. Power, **119**(4), pp. 674-682.

[9] Burshid, S.M., 1990, "Experimental Evaluation of Rotordynamic Coefficients for Hybrid Metal Mesh Pocket Damper Seals in Turbomachinery," M.S. Thesis, Texas A&M University.

[10] Choudhry, V., and Vance, J. M., 2005, "Design Equations for Wire Mesh Bearing Dampers in Turbomachinery," ASME Paper No. GT 2005-68641.

[11] Ertas, B. H, and Luo, H., 2007, "Nonlinear Dynamic Characterization of Oil-Free Mesh Dampers," ASME Paper No. DETC2007/VIB-34655.

[12] Ertas, B. H., 2008, "Compliant Hybrid Journal Bearings using Integral Wire Mesh Dampers," ASME Paper No. GT 2008-50984.

[13] Larue, G. D., Kang, S. G., and Wick, W., 2006, "Turbocharger with Hydrodynamic Foil Bearings," US Patent No. 7108488 B2.

[14] Young's Modulus of Copper, http://www.engineeringtoolbox.com, accessed May 19, 2008

[15] Properties of Copper, http://www.webelements.com, accessed Apr. 30, 2008

[16] Breedlove, A. W., 2007, "Experimental Identification of Structural Force Coefficients in a Bump-Type Foil Bearing," M.S. Thesis, Texas A&M University.

[17] Ginsberg, J. H., 2001, *Mechanical and Structural Vibration – Theory and Application*, John Wiley and Sons, New York, pp. 135-137.

[18] DellaCorte, C., 1997, "A New Foil Air Bearing Test Rig for Use to 700°C and 70,000 rpm," NASA TM-107405.

[19] Coleman, H., and, Steele, W., 1985, *Experimentation and Uncertainty Analysis for Engineers*, Wiley - Interscience Publications, New York, pp. 33-35.

APPENDIX A. MANUFACTURING OF TOP FOIL FOR METAL MESH BEARING

A 0.075 mm (3 mil) thick stainless steel strip, with a 93 mm length and a 28 mm width is taken as the raw material to prepare the top foil. The width, 28mm, of the top foil is the same as the width of the bearing cartridge. The flat steel strip is heat treated (annealed/tempered) inside a special forming die (see Fig. A1) to form a curvature with a diameter slightly larger (29.3 mm) than that of the hollow test journal. The process involves wrapping the flat top foil around a mandrel and holding it in place using a clamp. The entire apparatus is then heat treated according to the process mentioned in Table A1. The flat strip maintains a curved shape after the annealing process. The material then undergoes a heat treatment process to regain its elasticity
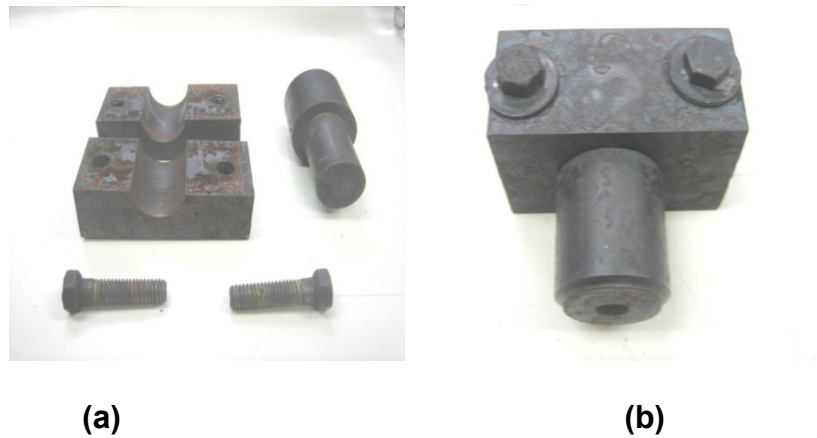

| (a) | (b) |

Figure A1. Apparatus for molding of top foil (a) Individual pieces (b) assembled structure

Table A1. Top foil heat treatment temperatures and times

Temperature	Time
1700 °F	10 minutes (apparatus is in furnace during warm-up)
1000 °F	16 hours
Furnace cooled	Until room temperature

Figure A2 presents (a) an initial flat metal strip and a formed smooth top foil, and (b) an installed top foil in the Metal Mesh.
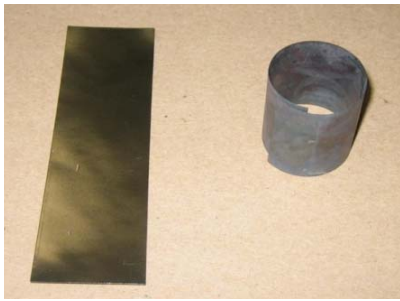
(a)   (b)

Figure A2. (a) Initial flat metal sheet and the formed smooth top foil and (b) installation of top foil within the metal mesh

Figure A3 shows a photograph of the Metal Mesh Foil Bearing constructed for the test rig (also used in the static and dynamic load tests).
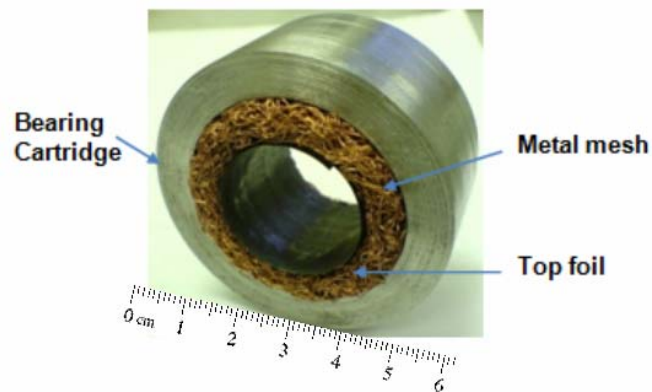

Figure A3. Photograph of constructed MMFB

APPENDIX B: CALIBRATION OF EDDY CURRENT SENSOR

Figure B1 shows the calibration graph for the eddy current sensor (ECS) with the bearing cartridge as the target material. The digital readout on a lathe displays the calibration displacement. The linear fit of the voltage versus displacement data gives an equation with its slope as the gain of the eddy current sensor. The R^2 term represents the goodness of fit between the line fit and the measured data.

$$V \text{ (V)} = 8.242 \, X \text{ (V/mm)} - 1.370 \text{ (V)}$$
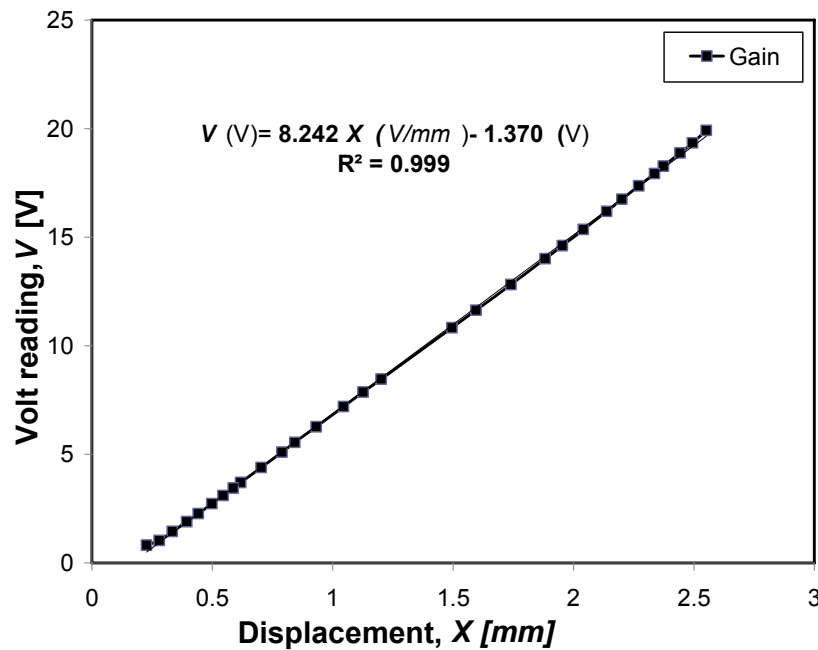$$R^2 = 0.999$$

Figure B1. Eddy current sensor calibration for steel bearing cartridge

The gain of the eddy current sensor found out using the digital display is 8.24 V/mm (209 mV/mil).

APPENDIX C. COST OF EQUIPMENT AND INSTRUMENTATION

Table C1 details the specification and cost for equipments and instrumentation purchased for

the air turbine driven gas bearing test rig.

Table C1.Specification and Cost of equipment and instrumentation

| Item	Specification	Vendor	Model#	Total Price	Delivery Date	URL
Tachometer	Tachometer/ totalizer includes NIST 115 V ac power	Monarch	ACT-3/115	$575	1/24/2008	www.monarchinstrument.com
Foam Anti-vibration Padding	CCS 1/2 x 48 x 36	Bryan Hose & Gasket	-	$64.80	1/31/2008	-
Test Journal	AISI 4140	Texas Transportation Institute	-	$475	2/11/2008	-
Alloy Steel Cup Point Socket Set Screw,	1-64 thread, 1/4" length, Pack of 10	McMaster-Carr	-	$6.94	2/18/2008	www.mcmaster.com
Positioning table, two encoders and Two Axis Readout	3" X3" travel 25 lb load capacity 1μm resolution	Velmex	AXY4009W1 585271-02 QC-120-AR	$3631	3/25/2008	www.velmex.com/man_axy40.htm
Flat Steel Plate	1" x 6" x 16"	Mack Bolt and Screw	-	$60	4/14/2008	-

TOTAL COST   **$4,813**

APPENDIX D. DYNAMIC CHARACTERIZATION OF TC DRIVEN MMFB TEST RIG

Impact tests on the TC Test Rig identify the natural frequencies of various installed components. Figure D1 (a) shows the various peak amplitude vibrations for frequencies 72 Hz, 128 Hz and 256 Hz being excited due to an impact force in the vertical direction. Figure D1(b) shows peak vibration amplitudes for frequencies 128 Hz and 300 Hz The signal strength for vibrations generated due to impact force in horizontal direction is ~3 times larger than that due to the impact force in vertical direction. This indicates that the stiffness offered by the bearing in the turbocharger in the horizontal direction is ~3 times smaller than that in the vertical direction.
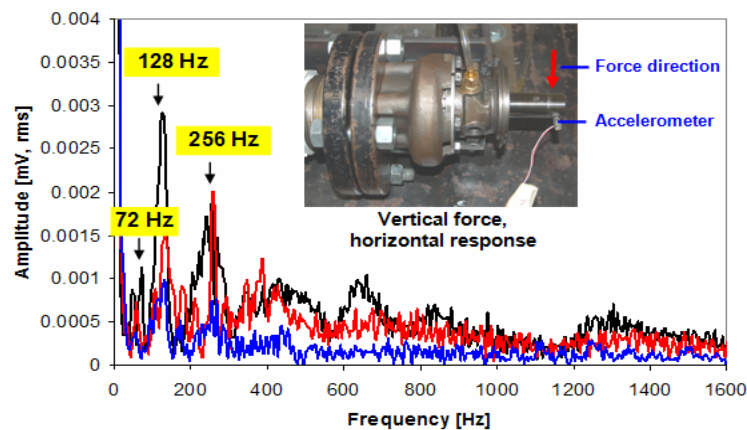
(a) Vertical impact force
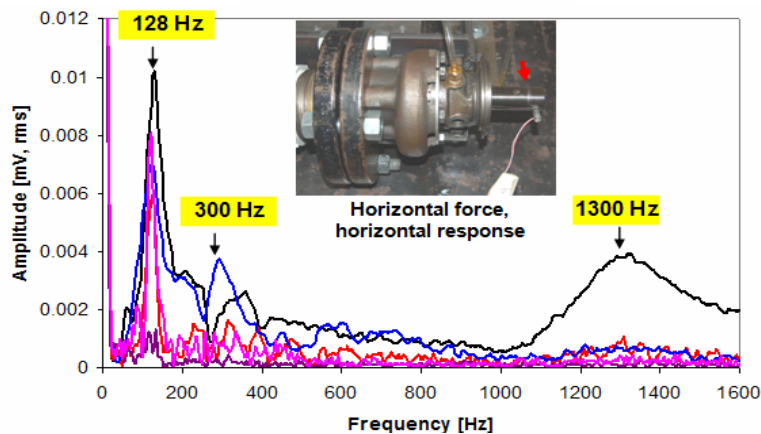
(b) Horizontal impact force

Figure D1. FFTs of transient responses of test journal to (a) vertical and (b) horizontal impact forces. Horizontal responses measured using accelerometer. Superposition of test data obtained during repeated tests

Figure D2 shows superimposed impact test data indicating two peak vibration amplitudes (60Hz, 108 Hz) due to axial impact force on the compressor plate.
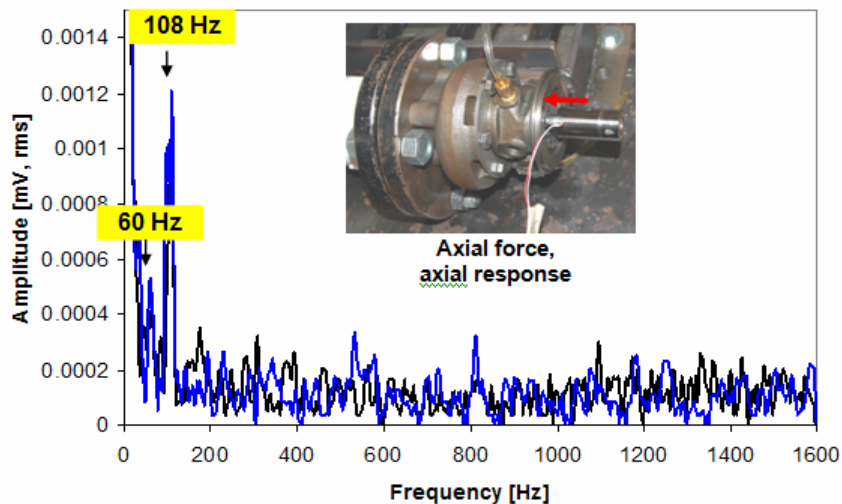

Figure D2. FFT of axial responses of compressor plate to axial impact forces. Axial responses measured using accelerometer. Superposition of test data obtained during repeated tests

Figure D3 shows the FFT of response of the turbocharger center housing due to radial impact forces on the compressor plate. The superimposed test data indicates three peak vibration amplitudes at frequencies 72 Hz, 108 Hz and 436 Hz.
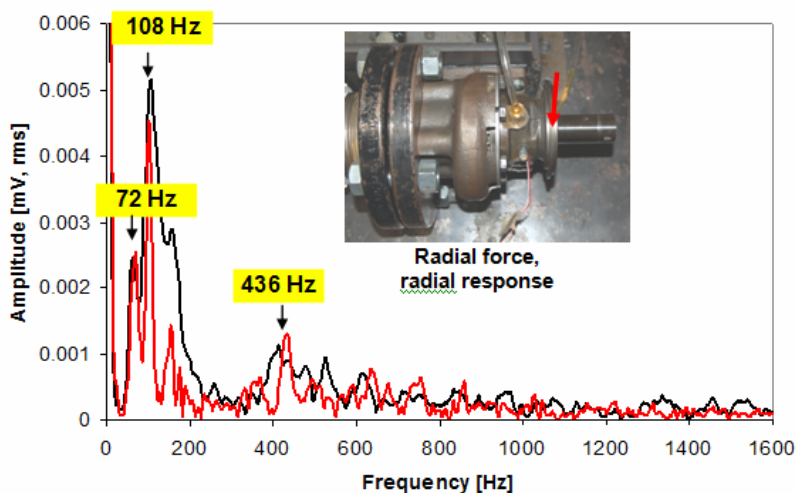

Figure D3. FFT of responses of turbocharger center housing to radial impact forces "on the compressor plate". Radial responses measured using accelerometer. Superposition of test data obtained during repeated tests

Figure D4 shows the superimposed transient responses for three impact tests on the turbine back plate with radial impact forces. The turbine backplate displays two peak vibration amplitudes at 72 Hz and 108 Hz.
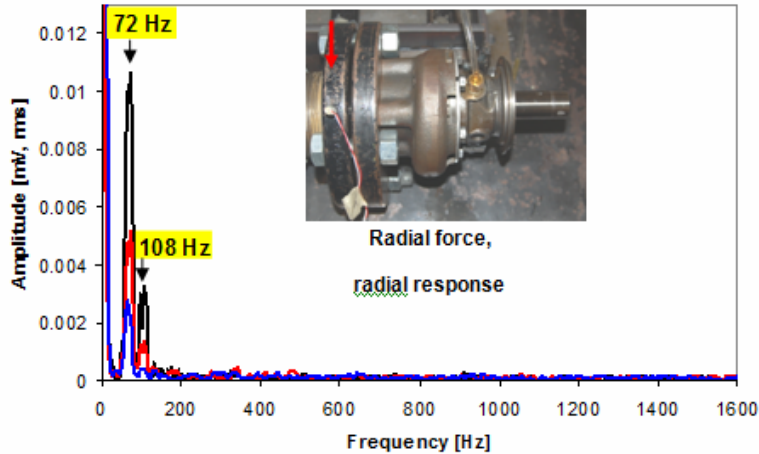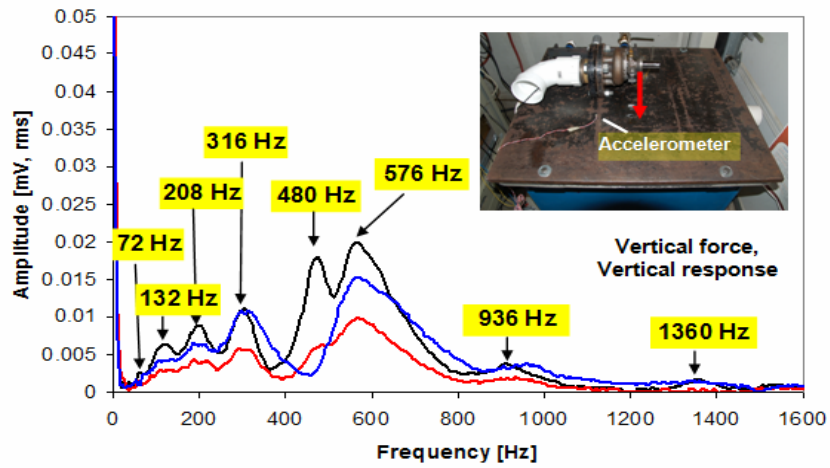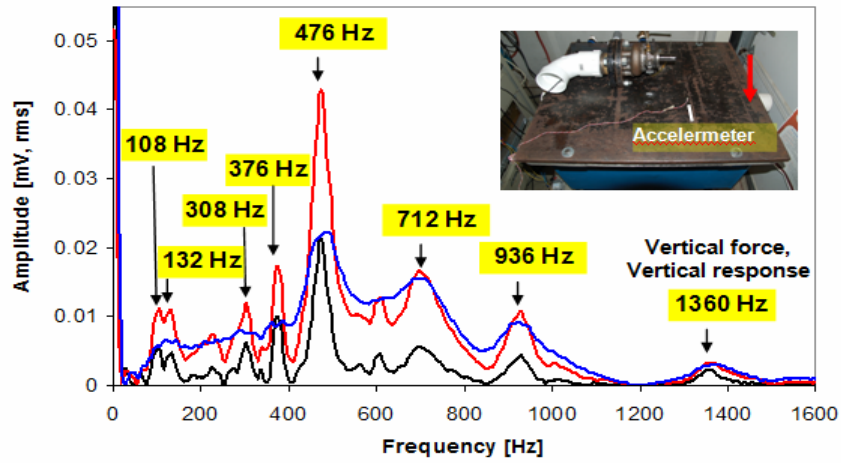

Figure D4. FFT of responses of turbine back plate to radial impact forces. Radial responses measured using accelerometer. Superposition of test data obtained during repeated tests

Figure D5 (a) shows the FFT of response of the test table due to an impact force on the left side of the table. Figure D5 (b) shows the FFT of response of the test table due to an impact force on the right side of the table. A large number of peak amplitudes are visible from the superimposed transient response data in the two figures. The excited frequencies are not necessarily due to the natural frequencies of the test table, but may be due to various other components installed on the table.

(a) Left side

(b) Right side

Figure D5. FFTs of responses of test table to vertical impact forces (a) test location 1: table left side and (b) test location 2: table right side. Vertical responses measured using accelerometer. Superposition of test data obtained during repeated tests